Structural and Multidisciplinary Optimization (2024) 67:179
https://doi.org/10.1007/s00158-024-03882-z

RESEARCH

Topology optimization with continuously varying load magnitude and direction for compliance minimization

Juana Gresia[1] · **Fernando Vasconcelos Senhora**[1] · **Glaucio H. Paulino**[2]

Received: 23 October 2023 / Revised: 8 August 2024 / Accepted: 30 August 2024 / Published online: 14 October 2024

Abstract

Traditional topology optimization methods only consider a limited number of loads in the optimization procedure, neglecting load variations common in real-world scenarios. To incorporate real load scenarios, robust topology optimization considers uncertainties in load directions while minimizing compliance, generating structures capable of withstanding variations in the load. This paper incorporates the angles of the load directions as parameters into the optimization formulation to design structures that perform well under a range of load directions. Additionally, the formulation is extended to incorporate local volume constraints to balance the solution distribution throughout a domain, achieving more complex designs with proper material distribution as the angle of the loads and the number of sub-regions increases while maintaining consistency in the worst-case scenario. Two and three-dimensional examples demonstrate that topology-optimized designs are susceptible to loads that vary in direction and magnitude, and by considering realistic loading conditions, this formulation yields robust, reliable designs, markedly enhancing their suitability for actual engineering applications.

Keywords Topology optimization · Compliance · Worst-case · Continuously varying load · Local constraints

List of Symbols

β	Parameter that controls the sharpness of the Heaviside projection function
Γ	Domain of admissible angles
ϵ	Ersatz stiffness
η	Threshold value for the Heaviside function
$\boldsymbol{\theta}$	Load angle
θ^{cr}	Critical angle
θ_{low}	Lower bound of the angle range
θ_r	Range of admissible angles
θ_{upp}	Upper bound of the angle range
ν	Poisson's ratio of solid material
$\tilde{\rho}$	Physical density vector
Ω	Design domain
$\mathop{\mathbb{A}}_{e=1}^{N_e}$	Assembly process of the global stiffness matrix
E_0	Young's modulus of solid material
$f(\mathbf{z}, \boldsymbol{\theta})$	Compliance
$\mathbf{F}(\boldsymbol{\theta})$	Load vector
$\mathbf{F}_f$	Load basis vector related to a fixed load
$\mathbf{F}_x, \mathbf{F}_y$	Load basis vectors
$g_V(\mathbf{z})$	Volume constraint
$\mathbf{K}(\mathbf{z})$	Stiffness matrix
$\mathbf{k}_0$	Local stiffness matrix of a solid element
$\mathbf{k}_e$	The eth element stiffness matrix
N_e	Number of elements
p	SIMP penalization parameter
$\mathbf{P}$	Filter matrix
r	Filter radius
s	Filter exponent
s_{ij}	Quadratic compliance terms related to the crossed load basis terms
t_{ij}	Quadratic compliance terms of the load basis vector i and j
T_{ij}	Part of the expression for the compliance associated with the loads i and j
$\mathbf{u}(\mathbf{z}, \boldsymbol{\theta})$	Displacement vector
v_i	Area (for two-dimensional problems) or volume (for three-dimensional problems) of element i
$\mathbf{x}_i$	Position of the centroid of element i
$\mathbf{z}$	Vector of design variables

Responsible Editor: Jun Wu

✉ Glaucio H. Paulino
gpaulino@princeton.edu

[1] School of Civil and Environmental Engineering, Georgia Institute of Technology, 790 Atlantic Drive, Atlanta, GA 30332, USA

[2] Department of Civil and Environmental Engineering, Princeton University, Princeton, NJ 08544, USA

1 Introduction

Topology optimization is a powerful technique used to determine the optimal distribution of material within a given design domain to achieve desired structural performance objectives. One important objective in topology optimization is minimizing compliance, i.e., maximizing the stiffness of the structure. Traditionally, optimization approaches have focused on a limited set of load directions (Diaz and Bendsøe 1992; Lopes et al 2015; Picelli et al 2018; Lee et al 2012; Talischi et al 2012; Senhora et al 2022), addressing uncertainties of actual structural engineering applications such as stress (Senhora et al 2020; Giraldo-Londoño and Paulino 2020), eigenmodes (Li and Khandelwal 2017; Allaire and Michailidis 2018), fatigue (Holmberg et al 2014; Jeong et al 2015), and buckling (Deng and Suresh 2017; Ferrari and Sigmund 2019). However, actual structural engineering applications are subjected to more complex conditions such as time-dependent loading (Yun and Youn 2017), kinematic couplings (Jin and Zhang 2016), load transmission (Lu et al 2021), and variable boundary conditions (Sá et al 2022). In this work, we focus on load variation and uncertainties that are handled by considering multiple load directions in the topology optimization formulation leading to designs that exhibit improved resistance to realistic loading scenarios when compared to designs obtained with traditional optimization formulations. Previous works have explored various approaches to address the challenge of load uncertainty by implementing stochastic or worst-case-oriented deterministic methods (Ben-Tal and Nemirovski 2002).

Stochastic methods treat the load as a random variable with a known probability distribution, and the objective and/or constraints of the optimization problem are represented as probabilities. These methods have been extensively applied to compliance-based topology optimization problems. The uncertainties of loads incorporated in the optimization process can be related to location (Liu and Wen 2018; Wang and Gao 2020; Dunning et al 2011), boundary conditions (Guo et al 2013), and nodal variations (Guest and Igusa 2008; Yi et al 2013). Other uncertainties are related to geometry (Zhang and Kang 2017; Lazarov et al 2012), material and stiffness (Asadpoure et al 2011; Jalalpour et al 2013). Li et al (2014) propose a compliance-volume product that considers the compliance (structural stiffness) and volume objectives, their method balances structural performance and material usage. Zhou and Li (2006) propose an approach for structures subjected to multiple load cases using a fiber-reinforced composite material model, which considers the anisotropic behavior of composite materials, and the load uncertainty is incorporated in the structure's stiffness. Tootkaboni et al (2012) introduce an approach that employs polynomial chaos expansions to model uncertainties. James et al (2009) introduce a dynamic aggregation technique that efficiently combines the load cases into a single equivalent load, simplifying the optimization process. Liu et al (2011) present the guide-weight method, which utilizes guide weights to distribute the loads and optimize the structure's response under multiple loading conditions by implementing multiple constraints in the formulation. Rong et al (2017) propose a method that optimizes structural topology while satisfying displacement constraints. da Silva Smith (1997) propose a heuristic method incorporating local stability constraints into the optimization process.

Worst-case-oriented methods involve solving an optimization problem within a set of potential load cases defining the objective and/or constraint function using the worst-case scenario. For minimization problems, this method provides an upper bound for the objective function and ensures the satisfaction of constraints for any load case within the set of possibilities. Young et al (1999) and Xie and Steven (1994) use an optimization approach and consider multiple load cases with stress constraints by using a finite-element analysis for each load case. Csébfalvi (2018) address uncertainty in load directions through an iterative approach. Holmberg et al (2017) propose a game theory-based approach considering variations in load direction. Thore et al (2020) model the problem as a Stackelberg game instead of a zero-sum game and demonstrated that this interpretation ensures the existence of a solution. Recently, Senhora et al (2023) make use of the linear state equations and the bi-linear characteristics of the von Mises stress to derive an analytical solution for the worst-case stress caused by continuously varying loads.

In contrast to the previous work by Senhora et al (2023) that focused on the stress constraint problem, this work uses linear state equations and the bi-linearity of the compliance function to obtain the solutions for the worst-case scenarios due to the continuously varying loads in the compliance minimization problem. The load-varying cases contemplated in this work are planar loads varying in magnitude and in a limited range of directions (Sect. 3.1), planar loads varying in direction combined with fixed loads (Sect. 3.2), two or more planar loads varying independently (Sect. 3.3), and loads varying in three dimensions (Sect. 3.4). The minimization of compliance is formulated considering the load variation in a worst-case-oriented approach. Furthermore, the formulation is extended to include local volume constraints, aiming to achieve a more balanced distribution of solutions across the domain and thereby enabling the creation of intricate designs with appropriate material distribution.

This paper is organized as follows: Sect. 2 presents the formulation of the minimization of compliance considering the variation of the load directions. Section 3 describes the aforementioned multiple load direction framework with

the derivations of the proposed analytic solutions for worst-case compliance. Section 4 extends the previously described method considering multiple sub-regions. Section 5 provides numerical examples obtained with the proposed method, and Sect. 6 presents the concluding remarks. Finally, the Appendix provides the convergence plots for selected numerical results.

2 Formulation

The compliance minimization optimization problem considering multiple load directions is stated as follows:

$$\begin{aligned} &\min_{\mathbf{z}\in\Omega}\max_{\theta\in\Gamma} f(\mathbf{z},\theta) = \mathbf{F}^T(\theta)\mathbf{u}(\mathbf{z},\theta) \\ &\quad s.t.\ g_V(\mathbf{z}) \le 0 \\ &\qquad 0 \le z_e \le 1, \quad e = 1,\dots,N_e \\ &\text{with}: \mathbf{K}(\mathbf{z})\mathbf{u}(\mathbf{z},\theta) = \mathbf{F}(\theta) \end{aligned} \tag{1}$$

where $f(\mathbf{z},\theta)$ is the compliance, $\mathbf{z}$ is the vector of design variables representing the material density at each point in the domain, and θ denotes the angular variation of the loading, $\mathbf{u}(\mathbf{z},\theta)$ is the displacement vector, $\mathbf{K}(\mathbf{z})$ is the stiffness matrix, $g_V(\mathbf{z})$ is the volume constraint and N_e is the number of elements. The linear state equation, $\mathbf{K}(\mathbf{z})\mathbf{u}(\mathbf{z},\theta) = \mathbf{F}(\theta)$, is employed, which right-hand side varies with the load angle, θ.

The stiffness of the elements is defined based on an element-based density approach using the Solid Isotropic Material with Penalization (SIMP) method (Bendsøe and Sigmund 1999; Bendsøe and Kikuchi 1988), and the stiffness matrix is composed as follows:

$$\begin{aligned} &\mathbf{K}(\mathbf{z}) = \mathop{\mathbb{A}}_{e=1}^{N_e} \mathbf{k}_e \\ &\text{with}: \mathbf{k}_e = [\epsilon + (1-\epsilon)\tilde{\rho}_e^p]\mathbf{k}_0 \end{aligned} \tag{2}$$

where $\mathbf{k}_e$ are the element stiffness matrices, $\mathop{\mathbb{A}}_{e=1}^{N_e}$ is the symbol that represents the assembly process of the global stiffness matrix, ϵ represents the Ersatz stiffness that prevents the stiffness matrix from becoming singular due to void regions, p is the SIMP penalization parameter that penalizes intermediate densities, $\mathbf{k}_0$ is the stiffness matrix for a solid element and $\tilde{\rho}$ is the physical density vector obtained by first applying a boundary-corrected *polynomial filter* (Senhora et al. 2023) as follows:

$$\begin{aligned} &P_{ij} = \frac{w_{ij}v_j}{\psi_i} \\ &\text{with}: w_{ij} = \max\left[0, \left(1 - \frac{\|\mathbf{x}_i - \mathbf{x}_j\|_2}{r}\right)\right]^s \end{aligned} \tag{3}$$

and

$$\psi_i = \begin{cases} \displaystyle\sum_{k=1}^{N_e} w_{ik}v_k, \ \text{(I)} \\ \max\left\{\displaystyle\sum_{k=1}^{N_e} w_{mk}v_k | m = 1,\dots,N_e\right\}, \ \text{(II)} \end{cases} \tag{4}$$

where Condition (I) is used if the element is less than the distance r from a boundary (load or support) assigned to it; otherwise, Condition (II) is used. Here, r is the filter radius, s represents the order of the filter (we employed $s = 1$), and $\|\mathbf{x}_i - \mathbf{x}_j\|_2$ is the distance between the centroids of the elements i and j. This filter effectively mitigates the boundary bias within the domain by implicitly functioning as a filler for empty elements, eliminating the need to explicitly introduce an outer layer of fill elements. Then, we apply the smooth Heaviside projection (Wang et al 2011) as follows:

$$\tilde{\rho} = \mathcal{H}(\mathbf{P}\mathbf{z}) = \frac{\tanh(\beta\eta) + \tanh(\beta(\mathbf{P}\mathbf{z} - \eta))}{\tanh(\beta\eta) + \tanh(\beta(1-\eta))} \tag{5}$$

where $\eta = 0.5$ is the value of the threshold for the Heaviside function, β controls the sharpness of such function, and $\mathbf{P}$ is the filter matrix that is computed applying the boundary-corrected *polynomial filter*.

3 Multiple load directions

In the topology optimization domain, the direction of the loads applied is represented by a variable $\theta \in \Gamma$, which represents the angle of the load in a set Γ of all possible angles. The solution of the worst-case scenario is represented by the maximum compliance of all possible angles, $\theta \in \Gamma$, and can be stated as an optimization problem:

$$\begin{aligned} &\max_{\theta\in\Gamma} f(\mathbf{z},\theta) \\ &\text{with}: \mathbf{K}(\mathbf{z})\mathbf{u}(\mathbf{z},\theta) = \mathbf{F}(\theta) \end{aligned} \tag{6}$$

The solution of the worst-case compliance is the critical angle, θ^{cr}. The following sections address the solution for the problem in Eq. 6 considering different sets of admissible load angles. For more information on the derivations of the worst-case approach in a stress-constrained setting, see Senhora et al (2023).

3.1 Case #1: planar load varying in an arbitrary range

This case considers a single load varying in direction within a limited range of angles, $\theta \in [\theta_{\text{low}}, \theta_{\text{upp}}]$, contained in the interval $[-\pi, \pi]$. The load is represented as the sum of two vectors weighted by cosine and sine functions:

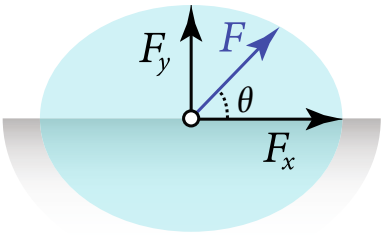

Fig. 1 **Case # 1**: domain of possible load cases (F, blue region) and the load basis vectors (F_x and F_y). When $\|F_x\| \neq \|F_y\|$, as a general case, an ellipsoid domain is generated, and when $\|F_x\| = \|F_y\|$, as a particular case, a circular domain is generated

$$\mathbf{F}(\theta) = \mathbf{F}_x \cos(\theta) + \mathbf{F}_y \sin(\theta) \tag{7}$$

where $\mathbf{F}_x$ and $\mathbf{F}_y$ are two linearly independent load basis vectors, which compose the space of admissible loads and are not necessarily aligned with any of the planar axes or have the same magnitude, as shown in Fig. 1.

As part of the algebraic manipulation, Eq. 7 is used in the equilibrium equation:

$$\begin{aligned}\mathbf{u}(\mathbf{z}, \boldsymbol{\theta}) &= \mathbf{K}^{-1}(\mathbf{z})\mathbf{F}(\boldsymbol{\theta}) \\ &= (\mathbf{K}^{-1}(\mathbf{z})\mathbf{F}_x)\cos(\theta) + (\mathbf{K}^{-1}(\mathbf{z})\mathbf{F}_y)\sin(\theta)\end{aligned} \tag{8}$$

Let's define $\mathbf{u}_x$ and $\mathbf{u}_y$ as follows:

$$\mathbf{u}_x = \mathbf{K}^{-1}(\mathbf{z})\mathbf{F}_x, \quad \mathbf{u}_y = \mathbf{K}^{-1}(\mathbf{z})\mathbf{F}_y \tag{9}$$

Such that, the compliance is computed as:

$$f(\mathbf{z}, \boldsymbol{\theta}) = [\mathbf{u}_x \cos(\theta) + \mathbf{u}_y \sin(\theta)]^T \mathbf{K}(\mathbf{z})[\mathbf{u}_x \cos(\theta) + \mathbf{u}_y \sin(\theta)] \tag{10}$$

The quadratic compliance terms are defined as:

$$t_{xx} = \mathbf{u}_x^T \mathbf{K}(\mathbf{z})\mathbf{u}_x, \quad t_{yy} = \mathbf{u}_y^T \mathbf{K}(\mathbf{z})\mathbf{u}_y, \quad t_{xy} = \mathbf{u}_x^T \mathbf{K}(\mathbf{z})\mathbf{u}_y \tag{11}$$

Which are replaced in Eq. 10:

$$f(\mathbf{z}, \boldsymbol{\theta}) = t_{xx}\cos^2(\theta) + t_{yy}\sin^2(\theta) + 2t_{xy}\cos(\theta)\sin(\theta) \tag{12}$$

This equation is simplified using trigonometric identities:

$$f(\mathbf{z}, \boldsymbol{\theta}) = 0.5[(t_{xx} - t_{yy})\cos(2\theta) + t_{xx} + t_{yy}] + t_{xy}\sin(2\theta) \tag{13}$$

The optimization problem for the critical load angle is written as follows:

$$\begin{aligned}&\max_{\theta \in \Gamma} f(\mathbf{z}, \boldsymbol{\theta}) \\ &\text{with} : \mathbf{K}(\mathbf{z})\mathbf{u}_x = \mathbf{F}_x, \quad \mathbf{K}(\mathbf{z})\mathbf{u}_y = \mathbf{F}_y\end{aligned} \tag{14}$$

The compliance in Eq. 13 is differentiated and set equal to zero, which leads to the following solution:

$$\theta^* = \theta^{cr} = \frac{1}{2}\tan^{-1}(2t_{xy}, t_{xx} - t_{yy}) \tag{15}$$

To generalize this solution for any angle range, first, we rotate the basis vectors F_x and F_y by an angle $(\theta_{\text{low}} + \theta_{\text{upp}})/2$ so that F_x lies in the middle of the interval $[\theta_{\text{low}}, \theta_{\text{upp}}]$ and $\theta_{\text{r}} = (\theta_{\text{upp}} - \theta_{\text{low}})/2$, as shown in Fig. 2. Thus, the solution of Eq. 14 is:

$$\theta^* = \theta^{cr} = \min\left\{\max\left[\frac{1}{2}\tan^{-1}(2t_{xy},\ t_{xx} - t_{yy}), -\theta_r\right], \theta_r\right\} \tag{16}$$

If we get a solution that satisfies the compliance for a range of $[-\theta_r, \theta_r]$, then the solution will also satisfy the compliance for $(\theta + \pi)$, in which $\theta \in [-\theta_r, \theta_r]$. This is known as the secondary range of admissible load angles (Senhora et al 2023), which occurs because the state equations are linear, and the compliance is a bilinear function. Notice that if we replace θ by $(\theta + \pi)$ in Eq. 13, we obtain:

$$\begin{aligned}f(\mathbf{z}, \boldsymbol{\theta} + \boldsymbol{\pi}) = 0.5[(t_{xx} - t_{yy})\cos(2\theta + 2\pi) + t_{xx} \\ + t_{yy}] + t_{xy}\sin(2\theta + 2\pi)\end{aligned} \tag{17}$$

since $\cos(2\theta + 2\pi) = \cos(2\theta)$ and $\sin(2\theta + 2\pi) = \sin(2\theta)$, the expression in Eq. 17 is numerically equivalent to the expression in Eq. 13.

3.2 Case #2: planar load varying 360° plus a fixed load

This case considers a load varying 360° and a fixed load that does not vary in direction. The loads are represented as:

$$\mathbf{F}(\boldsymbol{\theta}) = \mathbf{F}_x \cos(\theta) + \mathbf{F}_y \sin(\theta) + \mathbf{F}_f \tag{18}$$

where $\mathbf{F}_f$ is the load basis vector related to the fixed load. The schematic of this load case is presented in Fig. 3.

Let's define $\mathbf{u}_f = \mathbf{K}^{-1}\mathbf{F}_f$, together with the extra quadratic compliance terms:

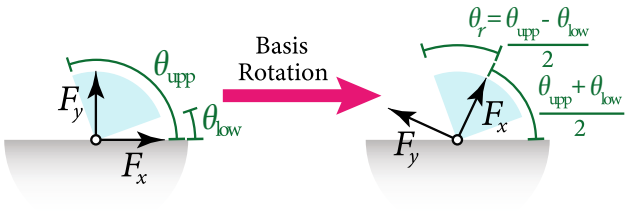

Fig. 2 Rotation of the basis vectors (F_x and F_y) for any continuous range of admissible angles

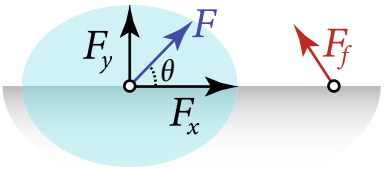

Fig. 3 **Case # 2**: domain of possible load cases (F, blue region), the load basis vectors (F_x and F_y) for the varying load and the fixed load (F_f, red). When $\|F_x\| \neq \|F_y\|$, as a general case, an ellipsoid domain is generated, and when $\|F_x\| = \|F_y\|$, as a particular case, a circular domain is generated

$$t_{ff} = \mathbf{u}_f^T \mathbf{K}(\mathbf{z})\mathbf{u}_f, \quad t_{xf} = \mathbf{u}_x^T \mathbf{K}(\mathbf{z})\mathbf{u}_f, \quad t_{yf} = \mathbf{u}_y^T \mathbf{K}(\mathbf{z})\mathbf{u}_f \tag{19}$$

Similarly to Case #1 (Sect. 3.1), the compliance is obtained as follows:

$$f(\mathbf{z},\boldsymbol{\theta}) = t_{xx}\cos^2(\theta) + t_{yy}\sin^2(\theta) + t_{ff} + 2t_{xy}\sin(\theta)\cos(\theta) + 2t_{xf}\cos(\theta) + 2t_{yf}\sin(\theta) \tag{20}$$

To simplify the expression in Eq. 20 we apply the Weierstrass variable substitution (Spivak 1965):

$$\sin(\theta) = \frac{2u}{1+u^2}, \quad \cos(\theta) = \frac{1-u^2}{1+u^2} \tag{21}$$

Which leads to the polynomial expression:

$$f(\mathbf{z},u(\boldsymbol{\theta})) = \frac{1}{(1+u^2)^2}\Big[t_{ff} + 2t_{xf} + t_{xx} + 4(t_{yf}+t_{xy})u + 4(t_{yf}-t_{xy})u^3 + 2(t_{ff}+2t_{yy}-t_{xx})u^2\Big] \tag{22}$$

The optimization problem for the critical load angle is:

$$\max_{u\in R} f(\mathbf{z},u(\boldsymbol{\theta})) \quad \text{with}: \mathbf{K}(\mathbf{z})\mathbf{u}_x = \mathbf{F}_x, \quad \mathbf{K}(\mathbf{z})\mathbf{u}_y = \mathbf{F}_y, \quad \mathbf{K}(\mathbf{z})\mathbf{u}_f = \mathbf{F}_f \tag{23}$$

To get the solution to the problem in Eq. 23, we differentiate the objective function with respect to the optimization variable (u) as follows:

$$\frac{\partial f(\mathbf{z},u(\boldsymbol{\theta}))}{\partial u} = \frac{4(t_{xy}+t_{yf}) + 4(t_{xy}-t_{yf})u^4}{(1+u^2)^3} + \frac{8(t_{yy}-t_{xx}-t_{xf})u - 24t_{xy}u^2}{(1+u^2)^3} + \frac{8(t_{xx}-t_{yy}-t_{xf})u^3}{(1+u^2)^3} = 0 \tag{24}$$

where u^* are the roots of the fourth-degree polynomial in Eq. 24, and the solution is the one that gets the maximum value of compliance.

3.3 Case #3: multiple independent loads with varying angles

This case considers several loads varying independently of each other, and the variable that controls the angle of the loads, θ, is a vector in $[-\pi,\pi]^n$, where n is the number of loads, and each component of this vector controls the angle of the various loads. First, the problem is solved by considering two loads with two independent angles ($n = 2$), and then the solution is generalized for n-number of loads. For the particular case $n = 2$, the loads are represented as:

$$\mathbf{F}(\boldsymbol{\theta}) = \mathbf{F}_1(\theta_1) + \mathbf{F}_2(\boldsymbol{\theta}_2) \tag{25}$$

where

$$\mathbf{F}_1(\theta_1) = \mathbf{F}_{1x}\cos(\theta_1) + \mathbf{F}_{1y}\sin(\theta_1)$$
$$\mathbf{F}_2(\theta_2) = \mathbf{F}_{2x}\cos(\theta_2) + \mathbf{F}_{2y}\sin(\theta_2) \tag{26}$$

Notice that $\mathbf{F}_1$ and $\mathbf{F}_2$ are the load components that vary in direction with θ_1 and θ_2, respectively. The schematic of this load case is presented in Fig. 4.

Let's define $\mathbf{u}_{1x}$, $\mathbf{u}_{1y}$, $\mathbf{u}_{2x}$ and $\mathbf{u}_{2y}$ as follows:

$$\mathbf{u}_{1x} = (\mathbf{K}^{-1}\mathbf{F}_{1x}), \quad \mathbf{u}_{1y} = (\mathbf{K}^{-1}\mathbf{F}_{1y})$$
$$\mathbf{u}_{2x} = (\mathbf{K}^{-1}\mathbf{F}_{2x}), \quad \mathbf{u}_{2y} = (\mathbf{K}^{-1}\mathbf{F}_{2y}) \tag{27}$$

As well as the following quadratic compliance terms:

$$\begin{aligned} t_{1xx} &= \mathbf{u}_{1x}^T\mathbf{K}(\mathbf{z})\mathbf{u}_{1x}, & t_{1yy} &= \mathbf{u}_{1y}^T\mathbf{K}(\mathbf{z})\mathbf{u}_{1y} \\ t_{2xx} &= \mathbf{u}_{2x}^T\mathbf{K}(\mathbf{z})\mathbf{u}_{2x}, & t_{2yy} &= \mathbf{u}_{2y}^T\mathbf{K}(\mathbf{z})\mathbf{u}_{2y} \\ t_{1xy} &= \mathbf{u}_{1x}^T\mathbf{K}(\mathbf{z})\mathbf{u}_{1y}, & t_{2xy} &= \mathbf{u}_{2x}^T\mathbf{K}(\mathbf{z})\mathbf{u}_{2y} \\ s_{xx} &= \mathbf{u}_{1x}^T\mathbf{K}(\mathbf{z})\mathbf{u}_{2x}, & s_{yy} &= \mathbf{u}_{1y}^T\mathbf{K}(\mathbf{z})\mathbf{u}_{2y} \\ s_{xy} &= \mathbf{u}_{1x}^T\mathbf{K}(\mathbf{z})\mathbf{u}_{2y}, & s_{yx} &= \mathbf{u}_{1y}^T\mathbf{K}(\mathbf{z})\mathbf{u}_{2x} \end{aligned} \tag{28}$$

Similarly to the previous cases, by making use of trigonometric identities, the compliance is rewritten as follows:

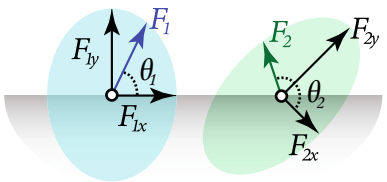

Fig. 4 **Case # 3**: domain of possible load cases (F_1, blue region and F_2, green region) and the load basis vectors (F_{1x}, F_{1y}, F_{2x} and F_{2y}). When $\|F_{1x}\| \neq \|F_{1y}\|$ or $\|F_{2x}\| \neq \|F_{2y}\|$, as a general case, an ellipsoid domain is generated, and when $\|F_{1x}\| = \|F_{1y}\|$ or $\|F_{2x}\| = \|F_{2y}\|$, as a particular case, a circular domain is generated

$$
\begin{aligned}
f(\mathbf{z},\boldsymbol{\theta}) = & t_{1xy}\sin(2\theta_1) + 0.5(t_{1xx}+t_{1yy}) \\
& + 0.5(t_{1xx}-t_{1yy})\cos(2\theta_1) \\
& + t_{2xy}\sin(2\theta_2) + 0.5(t_{2xx}+t_{2yy}) \\
& + 0.5(t_{2xx}-t_{2yy})\cos(2\theta_2) \\
& + (s_{yx}+s_{xy})\sin(\theta_1+\theta_2) \\
& + (s_{xx}-s_{yy})\cos(\theta_1+\theta_2) \\
& + (s_{yx}-s_{xy})\sin(\theta_1-\theta_2) \\
& + (s_{xx}+s_{yy})\cos(\theta_1-\theta_2)
\end{aligned}
\tag{29}
$$

Then, the corresponding optimization problem for the critical load angle is:

$$
\begin{aligned}
& \max_{\theta\in\Gamma} f(\mathbf{z},\boldsymbol{\theta}) \\
& \text{with}: \mathbf{K}(\mathbf{z})\mathbf{u}_{1x} = \mathbf{F}_{1x}, \quad \mathbf{K}(\mathbf{z})\mathbf{u}_{1y} = \mathbf{F}_{1y} \\
& \qquad\quad \mathbf{K}(\mathbf{z})\mathbf{u}_{2x} = \mathbf{F}_{2x}, \quad \mathbf{K}(\mathbf{z})\mathbf{u}_{2y} = \mathbf{F}_{2y}
\end{aligned}
\tag{30}
$$

To solve the optimization problem, the expression of the compliance in Eq. 30 is decomposed into three parts to get an analytic upper bound caused by the combined loads, i.e.

$$
\begin{aligned}
T_1 &= 0.5[(t_{1xx}-t_{1yy})\cos(2\theta_1) + t_{1xx} + t_{1yy}] + t_{1xy}\sin(2\theta_1) \\
T_2 &= 0.5[(t_{2xx}-t_{2yy})\cos(2\theta_2) + t_{2xx} + t_{2yy}] + t_{2xy}\sin(2\theta_2) \\
T_{12} &= (s_{yx}+s_{xy})\sin(\theta_1+\theta_2) + (s_{xx}-s_{yy})\cos(\theta_1+\theta_2) \\
&\quad + (s_{yx}-s_{xy})\sin(\theta_1-\theta_2) + (s_{xx}+s_{yy})\cos(\theta_1-\theta_2)
\end{aligned}
\tag{31}
$$

Notice that the maximum sum of these terms is less than or equal to the sum of the maximum of each term. Thus, an upper limit is defined, consisting of the sum of the maximum of each term:

$$
f(\mathbf{z},\boldsymbol{\theta}^*) = T_1^* + T_2^* + T_{12}^* \tag{32}
$$

The expressions for T_1 and T_2 are similar to Eq. 13. Thus, the solution of each expression is:

$$
\begin{aligned}
\theta_1^* &= \frac{1}{2}\tan^{-1}(2t_{1xy}, t_{1xx}-t_{1yy}) \\
\theta_2^* &= \frac{1}{2}\tan^{-1}(2t_{2xy}, t_{2xx}-t_{2yy})
\end{aligned}
\tag{33}
$$

To get the solution for the T_{12} term, it is separated into two terms:

$$
T_{12}(u,v) = T_{12u}(u) + T_{12v}(v) \tag{34}
$$

Each term depends only on $u = \theta_1 + \theta_2$ and $v = \theta_1 - \theta_2$, respectively, such that:

$$
\begin{aligned}
T_{12u}(u) &= (s_{yx}+s_{xy})\sin(u) + (s_{xx}-s_{yy})\cos(u) \\
T_{12v}(v) &= (s_{yx}-s_{xy})\sin(v) + (s_{xx}+s_{yy})\cos(v)
\end{aligned}
\tag{35}
$$

As usual, each expression in Eq. 35 is differentiated and set equal to zero, leading to the following solutions:

$$
\begin{aligned}
u^* &= \tan^{-1}(s_{yx}+s_{xy}, s_{xx}-s_{yy}) \\
v^* &= \tan^{-1}(s_{yx}-s_{xy}, s_{xx}+s_{yy})
\end{aligned}
\tag{36}
$$

For the solutions presented in this case, the range of one or both load angles can be restricted similarly to Case #1 (Sect. 3.1).

Let's consider $[-\theta_{1r}, \theta_{1r}]$ and $[-\theta_{2r}, \theta_{2r}]$ as the range of admissible angles for θ_1 and θ_2, respectively. Then, for each expression in Eq. 33, the solutions considering limited ranges are:

$$
\begin{aligned}
\theta_1^* &= \min\left\{ \max\left[\frac{1}{2}\tan^{-1}(2t_{1xy},\ t_{1xx}-t_{1yy}), -\theta_{1r} \right], \theta_{1r} \right\} \\
\theta_2^* &= \min\left\{ \max\left[\frac{1}{2}\tan^{-1}(2t_{2xy},\ t_{2xx}-t_{2yy}), -\theta_{2r} \right], \theta_{2r} \right\}
\end{aligned}
\tag{37}
$$

In addition, the admissible range for u and v can be constructed based on θ_{1r} and θ_{2r} as $-[(\theta_{1r}+\theta_{2r}), (\theta_{1r}+\theta_{2r})]$ for both u and v. Then, the solutions considering limited ranges are:

$$
\begin{aligned}
u^* &= \min\left\{ \max\left[\tan^{-1}(s_{yx}+s_{xy}, s_{xx}-s_{yy}), \right.\right. \\
&\qquad \left.\left. -(\theta_{1r}+\theta_{2r}) \right], (\theta_{1r}+\theta_{2r}) \right\} \\
v^* &= \min\left\{ \max\left[\tan^{-1}(s_{yx}-s_{xy}, s_{xx}+s_{yy}), \right.\right. \\
&\qquad \left.\left. -(\theta_{1r}+\theta_{2r}) \right], (\theta_{1r}+\theta_{2r}) \right\}
\end{aligned}
\tag{38}
$$

3.3.1 Generalization for $n \geq 2$

This approach can be generalized for an arbitrary number of loads represented by an arbitrary number of angles θ_i by defining an upper limit of the compliance as follows:

$$
f(\mathbf{z},\boldsymbol{\theta}) = \sum_{i=1}^{n}\left(T_i + \sum_{j=i+1}^{n} T_{ij} \right) \tag{39}
$$

This expression is separated by considering the terms (T_i) that depend exclusively on θ_i, and the terms (T_{ij}) between θ_i and θ_j, when $i \neq j$.

3.4 Case #4: load varying in three dimensions

This case considers the loads in three dimensions in which the loads can represent a whole surface of possible load directions varying in a plane but also in out-of-plane directions. The three cases combine two or more loads that vary independently in direction with appropriate bases as illustrated by Fig. 5.

In the first case, two independent loads are combined with the basis that forms orthogonal planes, generating a spherical load surface, as shown in Fig. 5a. In the second case, unlike the previous case, one of the loads only varies in intensity from $-F_x$ to F_x in a fixed direction, generating a cylindrical load surface, as shown in Fig. 5b. Finally, in the third case, the three loads only vary in intensity in fixed directions, generating a cubic load surface, as shown in Fig. 5c.

The solution of the cases consists of using the derivations of Case #3 (Sect. 3.3) and the generalization of the number of loads presented in Sect. 3.3.1, taking into account that the loads, composed as shown in Eq. 26, consider their components as the loads presented in each orthogonal plane.

4 Consideration of multiple sub-regions

Incorporating local constraints in topology optimization involves imposing restrictions on the distribution of material in specific regions, favoring the creation of redundant load paths. This approach ensures that even if one section of the structure experiences a failure or damage, other parts can seamlessly bear the additional loads, preventing catastrophic consequences. Integrating local constraints in topology optimization not only bolsters structural redundancy but also addresses safety concerns regarding structural integrity requirements not directly considered in the framework, such as variation of the load location, heterogeneity of material properties, or local failures (e.g. local buckling). This becomes particularly crucial in aerospace and civil engineering applications, where structural failures can have severe consequences.

We establish sub-regions of arbitrary geometries within the design domain to specify the local constraints by applying the *k*-means algorithm. This algorithm segregates the elements into a predetermined number of clusters of similar size. In this work, the clusters (sub-regions) are determined by the position of the centroid of each element. For example, Fig. 6 presents the Hook domain geometry with distinct elements grouped into sub-regions using the aforementioned *k*-means algorithm and a passive region defined around the support area.

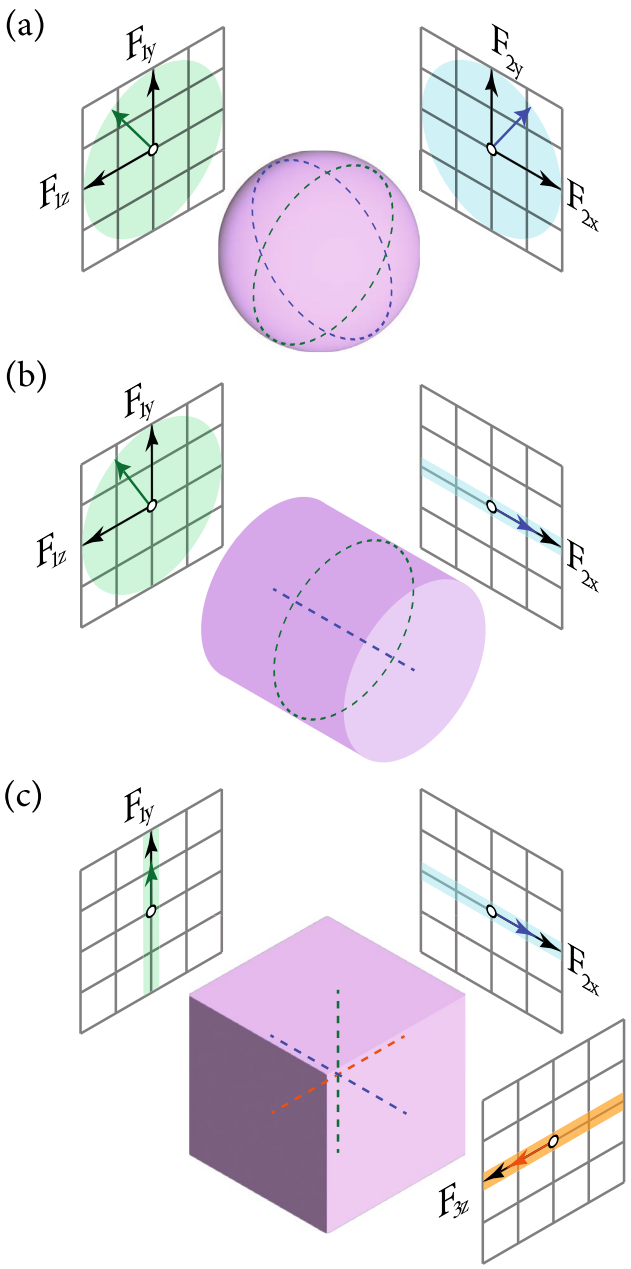

Fig. 5 **Case # 4**: combination of loads varying independently in magnitude and direction to get a load that varies in three dimensions. **a** Two independent loads that vary in magnitude and direction in orthogonal planes generate a spherical load surface. **b** Two independent loads in orthogonal planes, one varies in magnitude and direction, and the other varies just in magnitude, generate a cylindrical load surface. **c** Three independent loads in orthogonal planes varying in magnitude generate a cubic load surface

To accommodate the multiple volume constraints and passive regions in the optimized formulation, we utilize the optimization algorithm developed by Sanders et al (2018) that employs the ZPR design variable update scheme (Zhang et al 2018). This scheme takes advantage of the separability of the dual sub-problem, enabling us

to update the design variables independently for each constraint. Design variables within passive regions are not updated throughout the optimization and, as a result, remain unchanged after the initialization phase.

5 Results

This section presents the numerical results of a MATLAB implementation of the formulations described in Sect. 3 for two-dimensional structures (Hook and Pier cap beam) and a three-dimensional structure (Bridge). The two-dimensional examples are developed using the MATLAB code `PolyTop` (Talischi et al 2012), varying the objective and sensitivity functions according to each case. Similarly, in the three-dimensional example, we use linear hexahedral elements, which is consistent with the optimization framework based on linear elements (2D and 3D). For all examples, the Young's modulus and Poisson's ratio are $E_0 = 1$ and $\nu = 0.3$, respectively. In the optimization process, the stopping criterion is either the maximum number of iterations or the convergence tolerance of 0.01 (whichever is reached first). Convergence plots for selected numerical results are provided in the Appendix.

5.1 Hook

Figure 7 shows the Hook domain geometry, with a mesh that comprises 50,000 polygonal elements and a unitary distributed load, which can vary in angle (Case #1, Sect. 3.1). The optimization parameters are provided in Table 1.

5.1.1 Hook with global volume constraint and varying loads

Figure 8 illustrates the designs obtained for the Hook domain considering one distributed load varying with an angle θ for different ranges of admissible angle, θ_r. Notice that, as θ_r increases, the complexity of the design increases as well, with a tendency to concentrate material around the load region, in contrast to the standard case (Fig. 8c).

Figure 8c illustrates the standard case corresponding to the fixed downward load design ($\theta = -90°$). To provide context, we compare this solution with the Hook problem initially introduced by Talischi et al (2012) and optimized using `PolyTop`, as depicted in Fig. 8a. As expected, these solutions exhibit remarkable similarities due to their shared boundary conditions. Notable differences emerge primarily from the filtering and Heaviside projection techniques employed in this work (Sect. 2). Furthermore, we extend the comparison to the Hook problem approached via a ground structure method using GRAND (Zegard and Paulino 2014), presented in Fig. 8b. Evidently, there is a qualitative agreement between the solutions obtained through both methods.

In addition, when $\theta_r = 90°$ (Fig. 8g), the solution obtained for the worst-case scenario is $\theta^* = 79.4°$, implying that the results will remain consistent for any θ_r greater than θ^*, as evidenced in Fig. 8h. As expected, the compliance increases as θ_r increases, as shown in Fig. 9.

To verify that the continuously varying load approach outperforms the traditional single fixed load approach when considering multiple load directions, Fig. 10a displays the

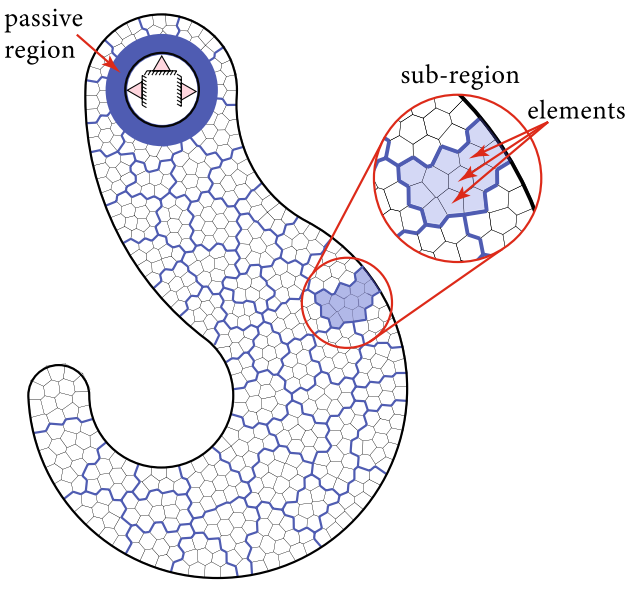

Fig. 6 Schematic of the Hook domain geometry with multiple local volume constraints, considering sub-regions defined by applying the *k*-means algorithm and a passive region around the support area

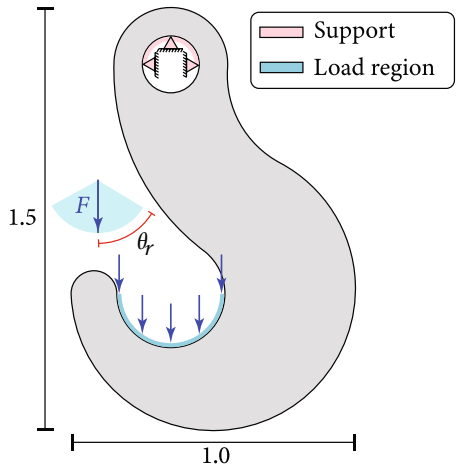

Fig. 7 Hook domain geometry and load conditions, corresponding to Case #1 (Sect. 3.1)

Table 1 Input parameters for the Hook domain problem

SIMP, penalty parameter p	1, 1.5, 2, 3, 4, 5, 6
Sharpness of Heaviside function, β	0.1
Material interpolation factor, γ[a]	1
Filter radius, r	0.012
Filter exponent, s	1
Volume fraction limit	0.4
Maximum number of iterations (per continuation step)	100

[a]This parameter is used when considering local volume constraints

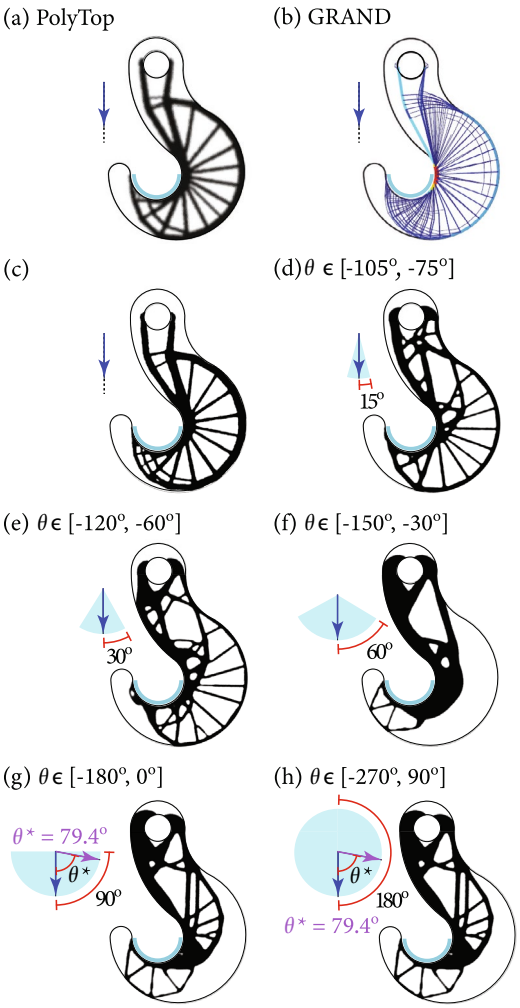

Fig. 8 Hook domain solutions considering one distributed load varying in direction, corresponding to Case #1 (Sect. 3.1). **a** Standard case solution using `PolyTop` (Talischi et al 2012). **b** Standard case solution using GRAND (Zegard and Paulino 2014). **c** Optimized design for a fixed downward load ($\theta = -90°$). **d** Optimized design for an angle range $\theta_r = 15°$. **e** Optimized design for an angle range $\theta_r = 30°$. **f** Optimized design for an angle range $\theta_r = 60°$. **g** Optimized design for an angle range $\theta_r = 90°$. **h** Optimized design for an angle range $\theta_r = 180°$

compliance of the optimized designs considering a single fixed load for different load directions in comparison to the optimized design compliance considering a continuously varying load (Case #1, Sect. 3.1). That is, for each point of the red curve, we have a different design for a different fixed load direction, while the blue curve represents a single structure designed with a continuously varying load and how the compliance of this single structure varies with the load direction.

Furthermore, Fig. 10b shows that, despite the fixed load design having lower compliance around the load angles considered in their optimization, the compliance for fixed load cases quickly degenerates, contrary to the compliance of the continuously varying load structure, which remains stable, presenting a lower compliance overall. Therefore, the optimized solution considering continuously varying load (Case #1, Sect. 3.1) can stand any variation in the load direction.

5.1.2 Hook with local volume constraints and varying loads

As previously stated in Sect. 5.1.1, the solutions tend to concentrate material around the distributed load, as shown in Fig. 8. To get solutions with more evenly distributed material, the optimized formulation incorporates local volume constraints, as described in Sect. 4. Further, a passive region (dark region) with a 0.05 thickness is considered around the support region, as shown in Fig. 11a.

Figure 11 illustrates the design obtained for the Hook domain considering global and local volume constraints with varying numbers of sub-regions (16, 24, 30, 48, and 54) and a distributed load varying with an angle θ for different ranges of admissible angle, θ_r. Notice that, as θ_r increases, the complexity of the design increases for each case (sub-regions) as well. Also, as the number of sub-regions increases, the designs present a more even material distribution in the

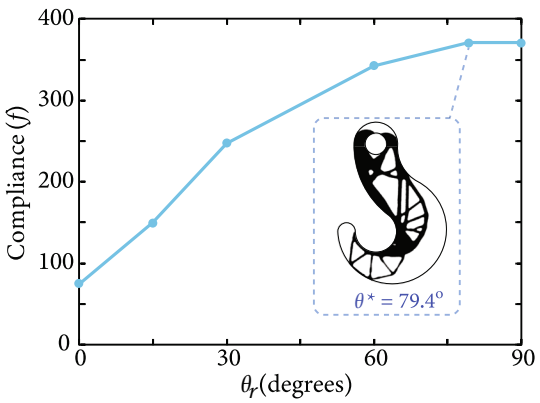

Fig. 9 Hook domain compliance obtained for different ranges of admissible angles, θ_r, considering Case #1 (Sect. 3.1)

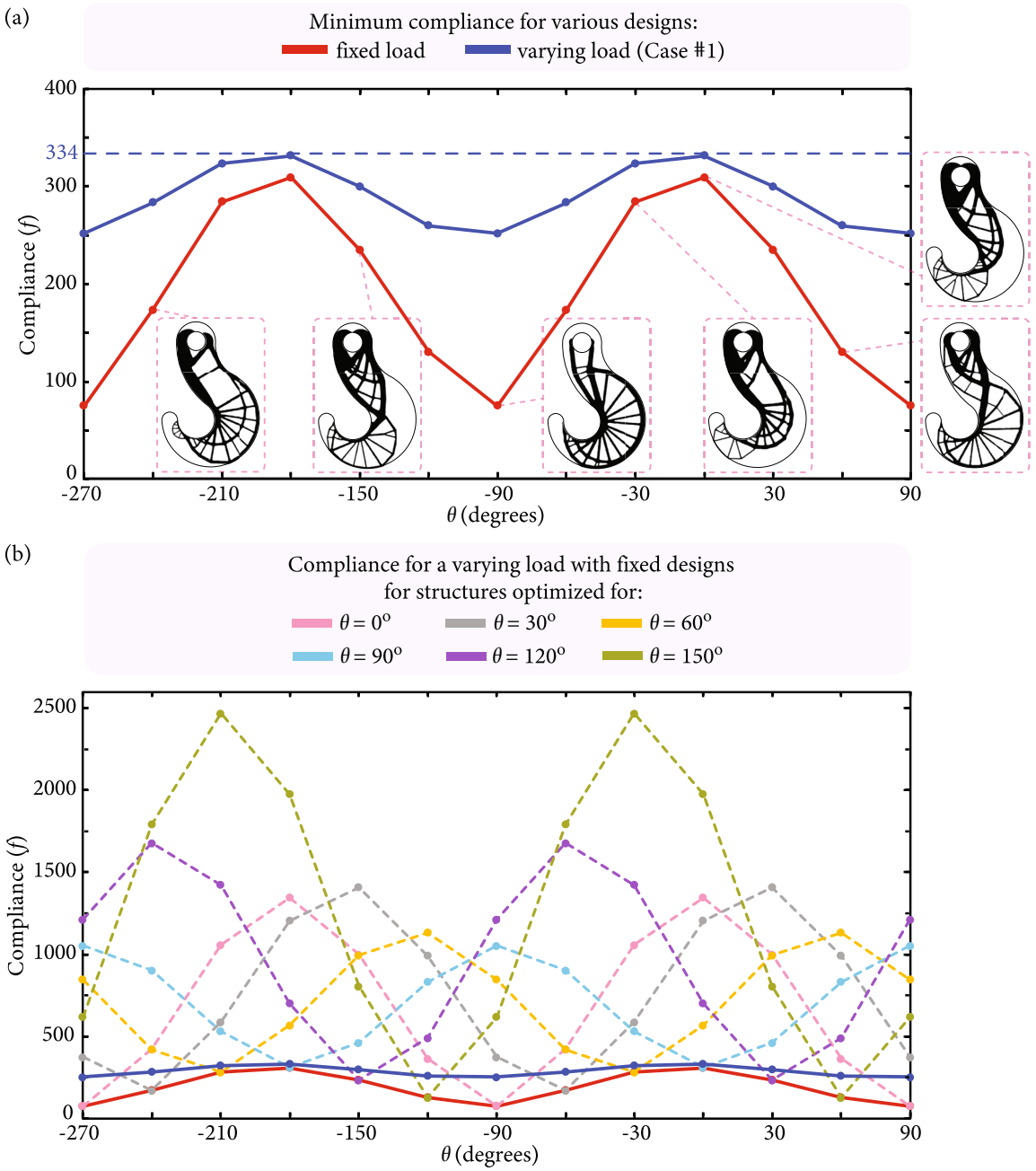

Fig. 10 Plot of the compliance of the Hook domain optimized designs considering several loading scenarios. **a** Compliance of the optimized designs considering a single fixed load for different load directions in comparison to the optimized design compliance considering a continuously varying load (Case #1, Sect. 3.1). That is, for each point of the red curve, we have a different design for a different fixed load direction, while the blue curve represents a single structure designed with the continuously varying load (Case #1, Sect. 3.1) and how the compliance of this single structure varies with the load direction. **b** Compliance of the fixed load designs in **a** as the load varies in direction. Each dotted line in this plot represents a single structure optimized for a fixed load direction and how its compliance changes with the load direction. This plot shows that, despite the fixed load design having lower compliance around the load angles considered in their optimization, the compliance for fixed load cases quickly degenerates, contrary to the compliance of the continuously varying load structure, which remains stable, presenting a lower compliance overall

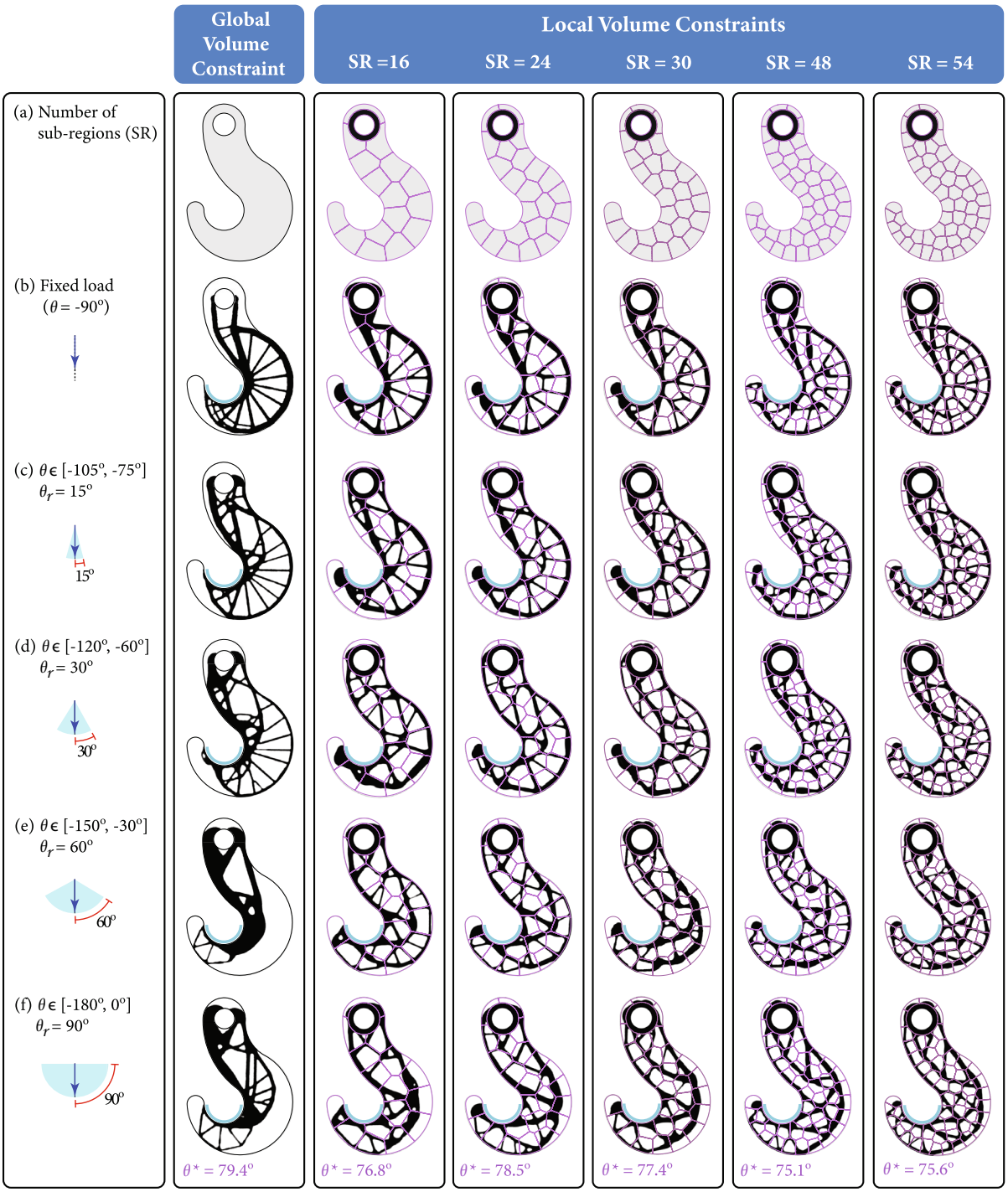

Fig. 11 Hook domain solutions considering global and local volume constraints with one distributed load varying in direction, corresponding to Case #1 (Sect. 3.1). **a** Hook domain geometry distribution for global and local volume constraints, considering a passive region (dark region) and varying numbers of sub-regions (SR). **b** Optimized designs for a fixed downward load ($\theta = -90°$). **c** Optimized designs for an angle range $\theta_r = 15°$. **d** Optimized designs for an angle range $\theta_r = 30°$. **e** Optimized designs for an angle range $\theta_r = 60°$. **f** Optimized designs for an angle range $\theta_r = 90°$

entire domain than those obtained considering global volume constraints.

We present the designs obtained for a fixed downward load ($\theta = -90°$) in Fig. 11b. We notice that the designs under the local volume constraints exhibit a greater prevalence of radial elements, with a concurrent reduction in the structural feature size in the lateral regions. Consequently, as the number of sub-regions increases, a more uniform size and distribution of elements across the Hook domain become evident.

In addition, for each case (sub-regions) when $\theta_r = 90°$, the solution obtained for the worst-case scenario θ^* is less than 90°, implying that the results will remain consistent for any θ_r greater than θ^*. Another interesting fact is that the value of the critical angle (θ^*) tends to decrease as the number of sub-regions increases. Figure 12 shows the compliance of each design with respect to θ_r, showing an increase in compliance as the number of sub-regions increases, as expected.

Figure 13 displays the average variation of the critical angle, θ^*, during each outer optimization iteration as the penalization factor is updated. This analysis corresponds to the results shown in Fig. 11f and considers a global volume constraint as well as two scenarios for the local volume constraint (16 and 48 sub-regions). In all cases, θ^* decreases with each outer iteration. The plot indicates that the total variation of θ^* is greatest for the global volume constraint and smallest for the local volume constraint with 48 sub-regions. This trend correlates with the convergence behavior of the objective function shown in Fig. 24, where the peaks of the objective function at each iteration are more pronounced in the global volume constraint case compared to the local volume constraint cases.

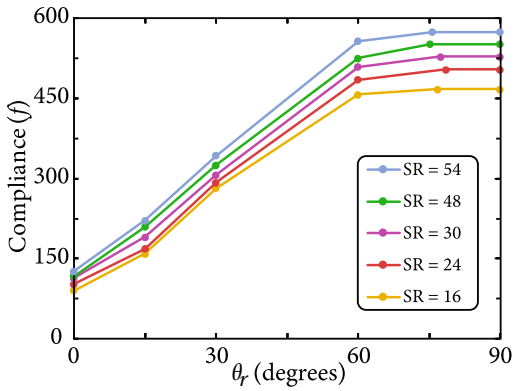

Fig. 12 Hook domain compliance considering local volume constraints with varying numbers of sub-regions (SR) and a passive region obtained for different ranges of admissible angles, θ_r, considering Case #1 (Sect. 3.1)

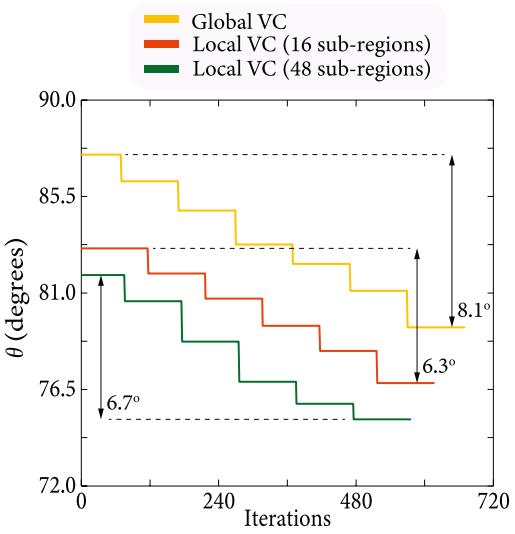

Fig. 13 Plot of the critical load angle (θ^*) variation for the Hook domain example considering global and local volume constraints with one distributed load varying in direction, corresponding to Case #1 (Sect. 3.1, Fig. 11f)

5.2 Pier cap beam

Figure 14 shows the Pier cap beam domain geometry with a 100,000 polygonal element mesh, presenting a symmetry with respect to the vertical center line. The domain presents two distributed loads, one on each side of the Pier cap beam. The optimization parameters are provided in Table 2.

5.2.1 Pier cap beam with a fixed load and a load varying in direction

Figure 15 illustrates the design obtained for the Pier cap beam considering one distributed load with a fixed direction, θ_1, combined with a simultaneous load varying with an angle θ_2.The results present an asymmetric material distribution in regard to the vertical center line despite the symmetric domain's geometry. This is prompted by the different load conditions on each side of the Pier cap beam, and it is more evident for fixed loads with directions below 90°, as shown in Figs. 15a–c.

Figure 16 illustrates the compliance results for optimized designs under two distinct scenarios: one with two fixed loads and the other with one fixed load and one continuously varying load (Case #2, Sect. 3.2). In both cases, the fixed loads are subjected to different load directions, resulting in significant variation in compliance as the load angle, θ, varies. Remarkably, it is evident that for every angle, θ, the compliance obtained for Case #2 (Sect. 3.2) consistently surpass those achieved when dealing with fixed load directions.

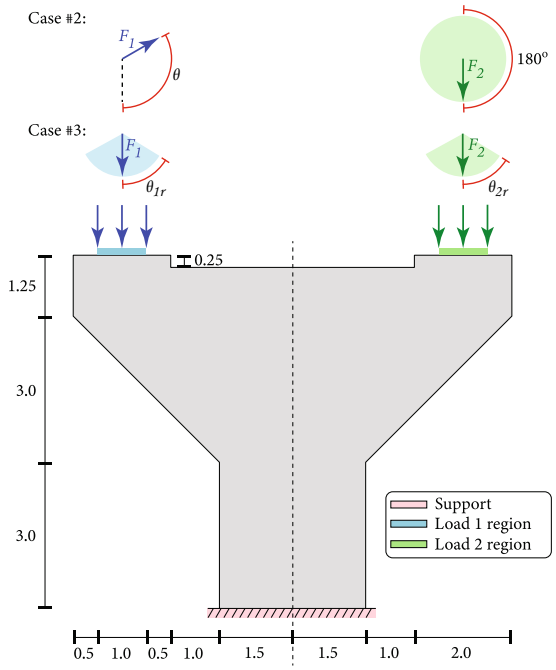

Fig. 14 Pier cap beam domain geometry and load conditions, corresponding to Case #2 (Sect. 3.2) and Case #3 (Sect. 3.3)

Table 2 Input parameters for the Pier cap beam domain problem

SIMP, penalty parameter p	1, 1.5, 2, 3, 4, 5, 6
Sharpness of Heaviside function, β	0.1
Filter radius, r	0.15
Filter exponent, s	1
Volume fraction limit	0.4
Maximum number of iterations (per continuation step)	100

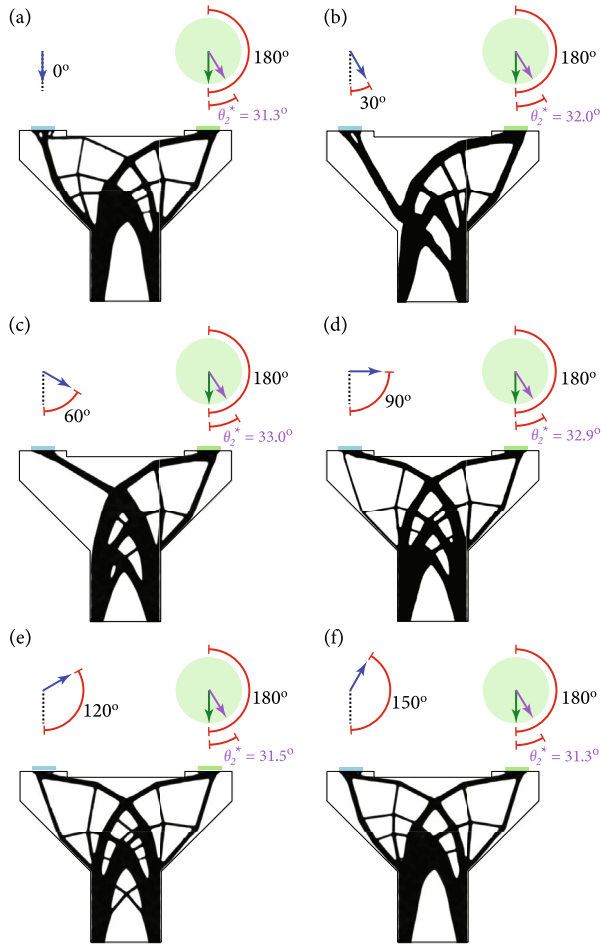

Fig. 15 Pier cap beam domain solutions considering one distributed load with fixed directions (θ_1, blue load), and one distributed load varying in direction (θ_2, green load), corresponding to Case #2 (Sect. 3.2). **a** Optimized design for a fixed load $\theta_1 = 0°$. **b** Optimized design for a fixed load $\theta_1 = 30°$. **c** Optimized design for a fixed load $\theta_1 = 60°$. **d** Optimized design for a fixed load $\theta_1 = 90°$. **e** Optimized design for a fixed load $\theta_1 = 120°$. **f** Optimized design for a fixed load $\theta_1 = 150°$

Moreover, when comparing the results in Fig. 16, there is an offset of 30° between them. This offset represents the solutions for the worst-case scenario θ_2^*, approximately 30° for each case as shown in Fig. 15. Additionally, these results converge at $\theta = -210°$ and $\theta = -30°$, presenting the same compliance. These angles denote the solutions for the worst-case scenario θ_1^* (assuming this load can vary in any direction), which are approximately 60° with respect to the downward direction ($\theta = -90°$) for each case as shown in Fig. 17.

5.2.2 Pier cap beam with two loads varying independently

Figure 17 presents the design obtained for the Pier cap beam considering two loads varying independently in direction with angles θ_1 and θ_2 for different ranges of admissible angle, θ_r. Notice that for each result, the material distribution tends to be symmetric with respect to the vertical center line. When $\theta_r = 60°$ (Fig. 17d), the solutions for the worst-case scenario are $\theta_1^* = 53.5°$ and $\theta_2^* = -53.6°$. Although these angles are below 60°, when $\theta_r = 90°$ (Fig. 17e) the solutions for the worst-case scenario are $\theta_1^* = 52.7°$ and $\theta_2^* = -52.1°$. Interestingly, even if θ_r increases, the designs obtained will remain consistent, as shown in Fig. 17f.

Moreover, for θ_r equalling or exceeding $\theta_r = 30°$, the designs obtained are similar or present very small differences (Figs. 17c–f) compared to those derived from smaller θ_r (Figs. 17a, b). Figure 18 displays the compliance corresponding to different θ_r, and it is noticed that as θ_r increases, the compliance does.

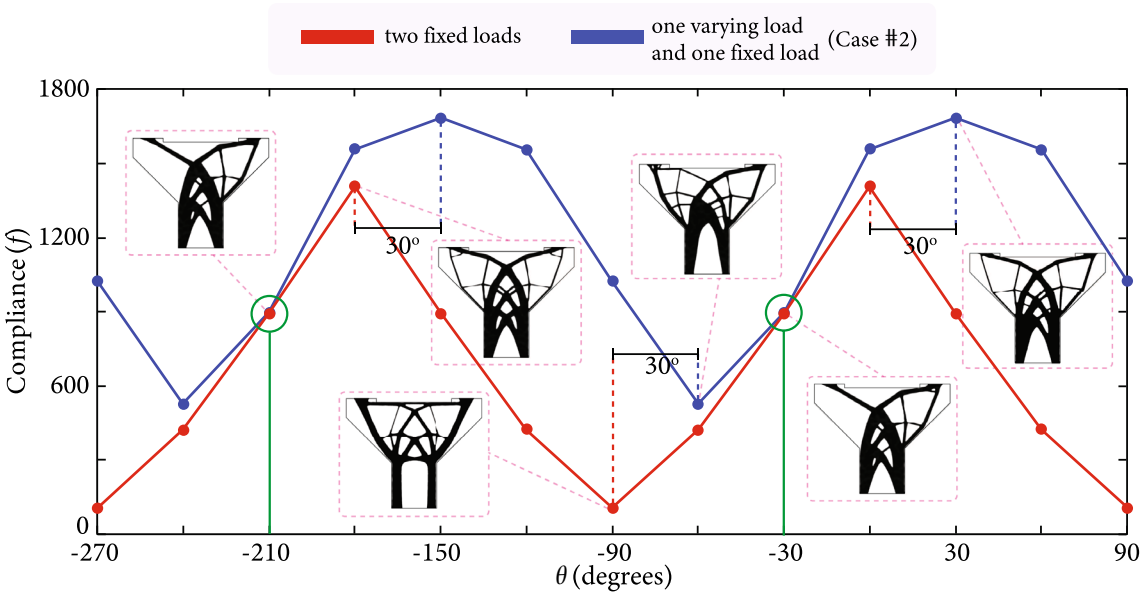

Fig. 16 Pier cap beam domain example: compliance of the optimized designs considering two fixed loads for different load directions in comparison to the optimized design compliance considering one fixed load and one continuously varying load (Case #2, Sect. 3.2). That is, for each point of both curves, we have different designs for different fixed load directions

To assess the efficacy of the approach, similarly to Case #1 (Sect. 3.1, Fig. 10), Fig. 19a displays the compliance of the optimized designs considering two fixed loads for different load directions in comparison to the optimized design compliance considering two continuously varying loads (Case #3, Sect. 3.3). In essence, the red curve represents distinct designs corresponding to different fixed load directions, while the blue curve represents a single structure optimized for continuously varying loads, showcasing how its compliance fluctuates with load direction changes. It is worth noting that compliance values for fixed loads exhibit significant fluctuations as the load angle, θ, shifts, with these values consistently lower than those observed in the worst-case scenario (Case #3, Sect. 3.3).

In addition, Fig. 19b shows that, despite the fixed load design having lower compliance around the load angles considered in their optimization, the compliance for fixed load cases rapidly degenerates, contrary to the compliance of the continuously varying load structure (Case #3, Sect. 3.3), which remains stable, presenting lower compliance overall, meaning that the efficacy of this approach can be extended to many loads applied in the domain.

Figure 20 illustrates the average variation of the critical angles, θ_1^* and θ_2^*, across each outer optimization iteration as the penalization factor is updated. Figure 20a corresponds to the results shown in Figs. 15a, c, and d, which consider a single distributed load with fixed directions ($\theta_1 = 0°$, 60° and 90°), and a single distributed load with a varying direction (θ_2), corresponding to Case #2 (Sect. 3.2). In all instances, θ_2^* exhibits only minor variations throughout the outer iterations, with a maximum angle variation of 1.4°. Similarly, Fig. 20b relates to the results presented in Fig. 17f, which considers two distributed loads varying independently in direction (θ_1 and θ_2), corresponding to Case #3 (Sect. 3.3). Notice that θ_1^* and θ_2^* decrease with each outer iteration, showing a maximum angle variation of 4.2°, which is greater than the variation observed in Case #2 depicted in Fig. 20a.

Moreover, these results align with the convergence behavior of the objective function shown in Figs. 25 and 26. Here, the peaks of the objective function at each iteration are noticeably less pronounced compared to the peaks observed for the Hook domain in Fig. 24, where angle variations are significantly greater, as shown in Fig. 13. Therefore, these findings provide evidence of the influence of the load angle variability on the optimization convergence.

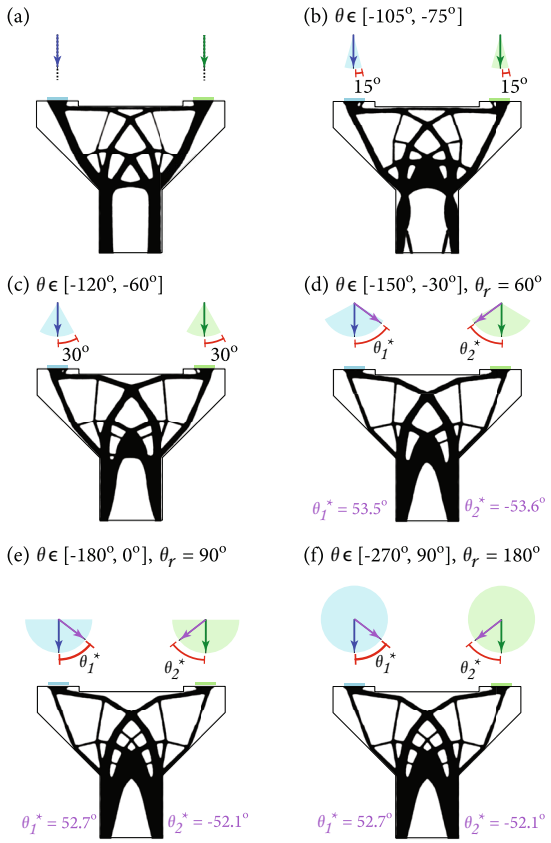

Fig. 17 Pier cap beam domain solutions considering two distributed loads varying independently in direction (θ_1 and θ_2, blue and green load, respectively), corresponding to Case #3 (Sect. 3.3). **a** Optimized design for fixed downward loads ($\theta = -90°$). **b** Optimized design for angle ranges $\theta_r = 15°$. **c** Optimized design for angle ranges $\theta_r = 30°$. **d** Optimized design for angle ranges $\theta_r = 60°$. **e** Optimized design for angle ranges $\theta_r = 90°$. **f** Optimized design for angle ranges $\theta_r = 180°$

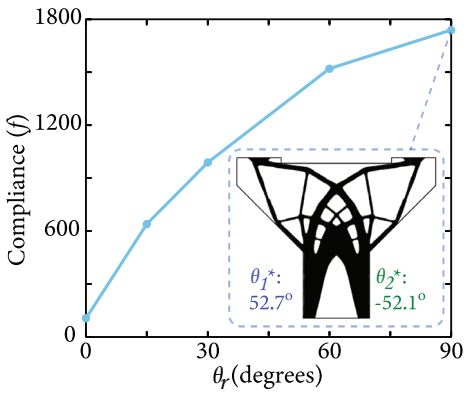

Fig. 18 Pier cap beam domain compliance obtained for different ranges of admissible angles, θ_r, considering Case #3 (Sect. 3.3)

5.3 Bridge

Figure 21 shows the Bridge domain geometry, along with the load, support, and passive region. This domain is meshed with 143,360 hexahedral elements. The optimization parameters are provided in Table 3.

Figure 22 illustrates the compliance obtained considering Case #4 (Sect. 3.4) for different ranges of admissible angles, θ_r. Notice that as θ_r increases, there is a clear difference between each case; specifically, for the worst-case solution ($\theta_r = 90°$), the compliance obtained for Case #4(b) is greater than the other cases. This is due to the lower volume yielded in Case #4(b), as shown in Fig. 23b.

Figure 23 presents the designs obtained for the Bridge domain considering two and three distributed independent loads in longitudinal and transversal orientations for which the bases form orthogonal planes. According to the variation in magnitude and direction, the load surfaces applied to the Bridge domain are: spherical, cylindrical, and cubic, related to Figs. 23a–c, respectively.

In Figs. 23a, b, the volume distribution typically exhibits symmetry around the vertical center line. As θ_r increases, there is a noticeable increase in volume concentration in the central region of the domain and at the base of the domain columns, respectively. On the other hand, in Fig. 23c, the volume distribution lacks symmetry in relation to the vertical center line. As θ_r expands, volume concentration is markedly increased within the columns of the Bridge domain.

6 Concluding remarks

This paper presents a topology optimization formulation that uses the linear state equations and the bi-linear properties of compliance to derive an analytic solution for the worst-case scenario caused by continuously-varying loads. These analytical solutions are obtained for different load conditions: two and three-dimensional loads, which can vary in an arbitrary range of angles, including direction and intensity. Furthermore, this formulation is extended to include local volume constraints to distribute material evenly across a domain, resulting in designs with improved redundancy as the angle of the loads and the number of sub-regions increase while maintaining consistency in worst-case scenario results. From the numerical examples, it becomes clear that designs considering only loads with fixed directions are vulnerable to variations in the load angle, implying that the structure may not adequately account for uncertainties and variations commonly seen in real-world applications. Conversely, considering a range of loads leads to different optimized designs

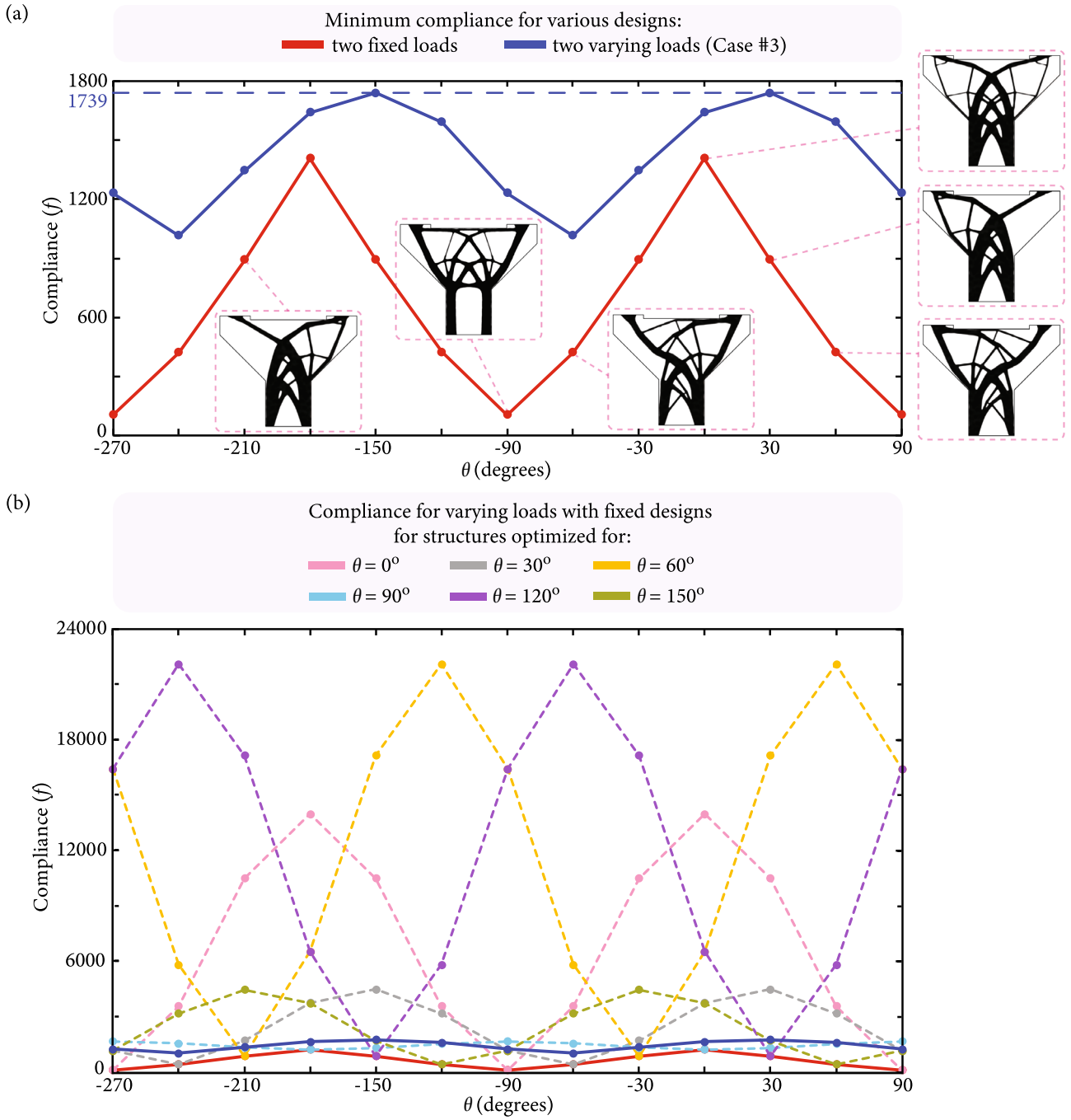

Fig. 19 Plot of the compliance of the Pier cap beam domain optimized designs considering several loading scenarios. **a** Compliance of the optimized designs considering two fixed loads for different load directions in comparison to the optimized design compliance considering two continuously varying loads (Case #3, Sect. 3.3). That is, the red curve represents distinct designs corresponding to different fixed load directions, while the blue curve represents a single structure optimized for continuously varying loads (Case #3, Sect. 3.3), showcasing how its compliance fluctuates with load direction changes. **b** Compliance of fixed loads designs in **a** as the loads vary in direction. Each dotted line in this plot represents a single structure optimized for fixed load directions and how its compliance changes with the load directions. This plot shows that, despite the fixed load design having lower compliance around the load angles considered in their optimization, the compliance for fixed load cases rapidly degenerates, contrary to the compliance of the continuously varying load structure, which remains stable, presenting a lower compliance overall

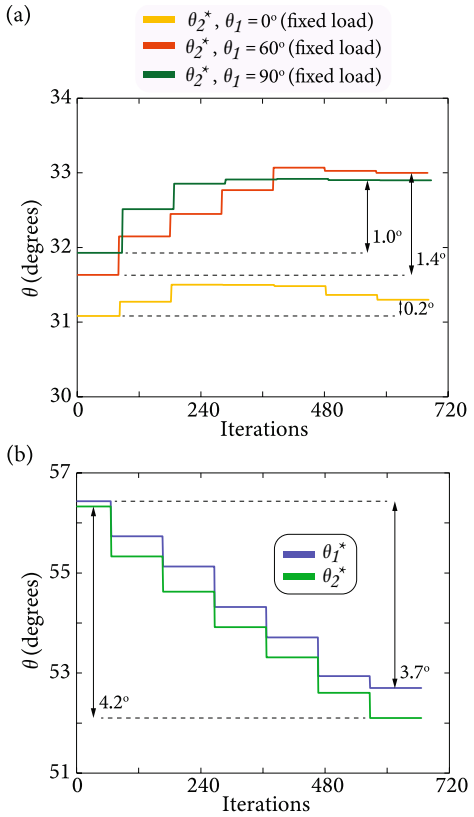

Fig. 20 Plot of the variation of the critical load angles (θ_1^* and θ_2^*) for the Pier cap beam domain example considering: **a** one distributed load with fixed directions (θ_1), and one distributed load varying in direction (θ_2), corresponding to Case #2 (Sect. 3.2, Fig. 15a, c and d). **b** Two distributed loads varying independently in direction (θ_1 and θ_2), corresponding to Case #3 (Sect. 3.3, Fig. 17f)

that are closer to realistic ones and robust under load direction variations. Therefore, this topology optimization formulation facilitates the design of structures capable of handling variations in load directions, enhancing performance and reliability. Future work could expand the continuously-varying load cases to nonlinear state equations, e.g., hyper-elastic materials, by taking advantage of local linearization of the respective objective/constraint functions, applying stochastic methods, or using data-driven approaches.

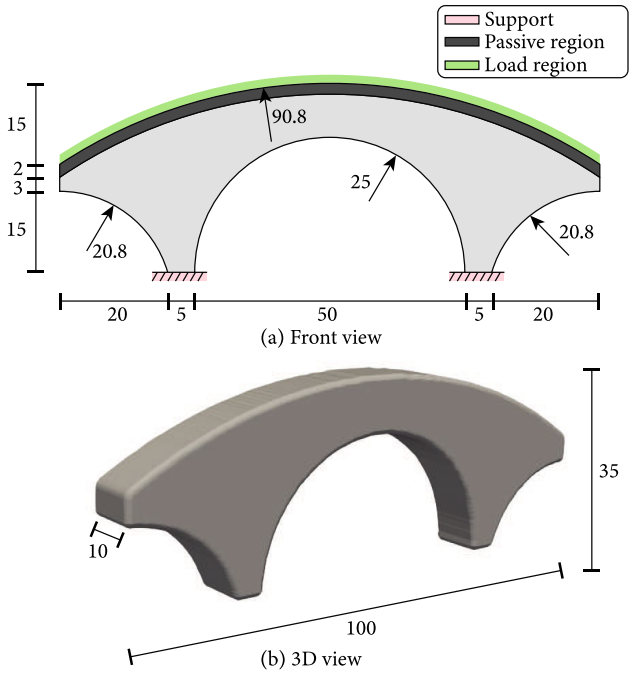

Fig. 21 **a** Front view of the Bridge domain geometry and load conditions, corresponding to Case #4 (Sect. 3.4). **b** Three-dimensional view of the Bridge domain geometry

Table 3 Input parameters for the Bridge domain problem

SIMP, penalty parameter p	1, 1.5, 2, 3, 4
Sharpness of Heaviside function, β	0.1
Filter radius, r	1
Filter exponent, s	1
Volume fraction limit	0.4
Maximum number of iterations (per continuation step)	200

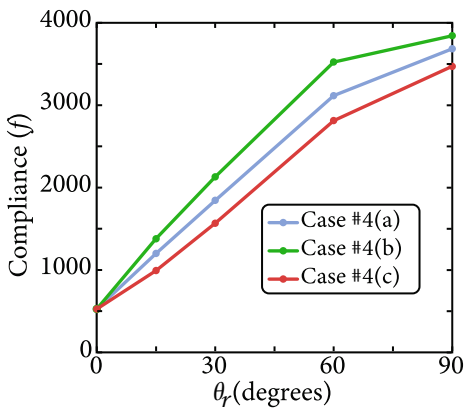

Fig. 22 Bridge domain compliance obtained for different ranges of admissible angles, θ_r, considering Case #4(a)–(c) (Sect. 3.4)

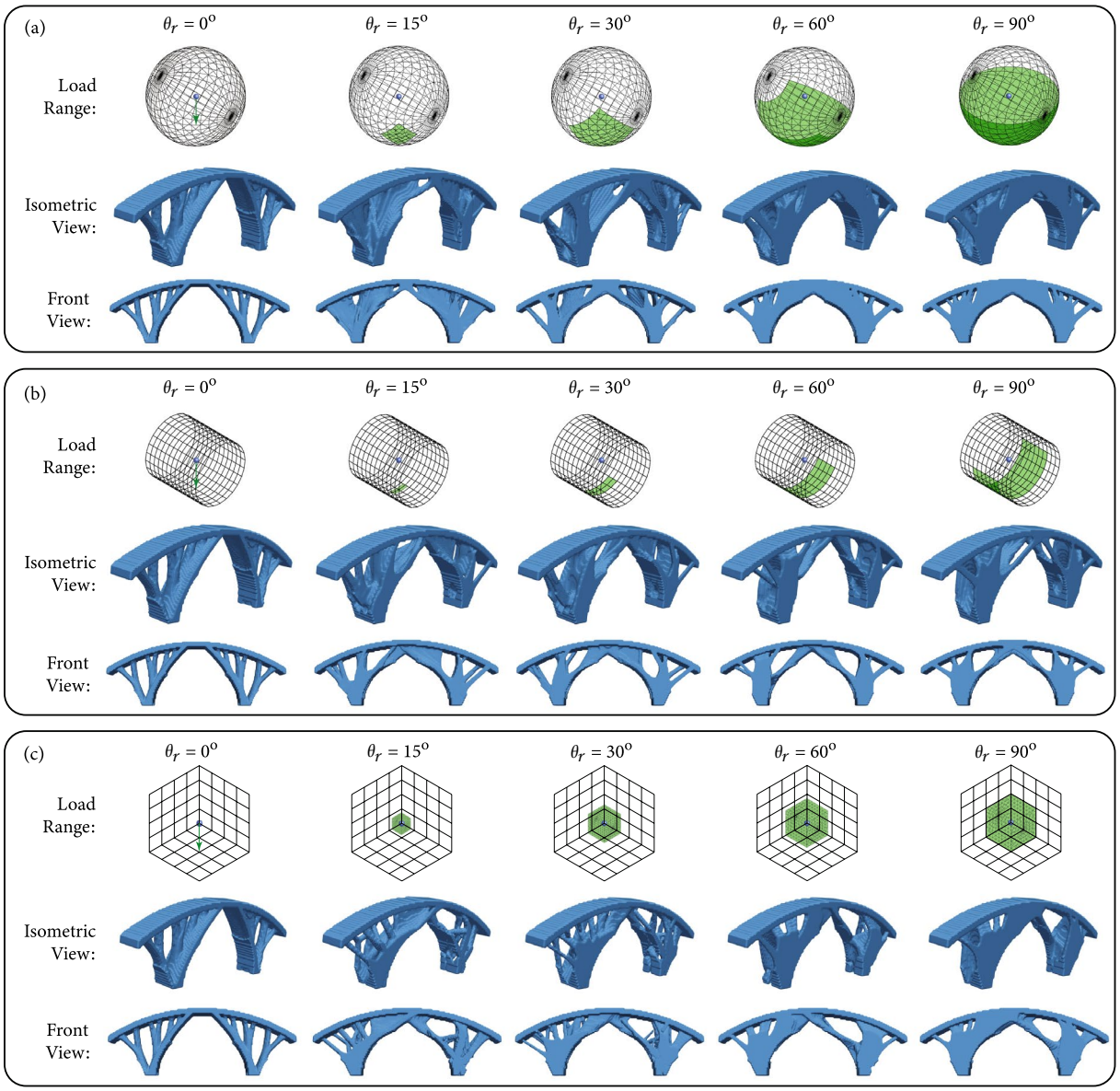

Fig. 23 Bridge domain solutions considering loads varying in three dimensions, corresponding to Case #4 (Sect. 3.4). Isometric and front view of the optimized designs for different ranges of admissible angles, θ_r, considering: **a** independent loads varying in magnitude and direction in orthogonal planes generating a spherical load surface. **b** Independent loads in orthogonal planes, one varying in magnitude and direction, and the other varying just in magnitude, generating a cylindrical load surface. **c** Independent loads varying in magnitude in orthogonal planes generating a cubic load surface

Appendix: Convergence of the optimization approach

The convergence plots of the optimization approach for the Hook example are displayed in Fig. 24, and for the Pier cap beam example are displayed in Figs. 25 and 26. In each plot, the objective function (compliance) is shown as a function of the optimization iterations. The peaks are caused at every outer iteration when the penalization factor is updated. However, despite the peaks, the convergence is consistently smooth across all cases.

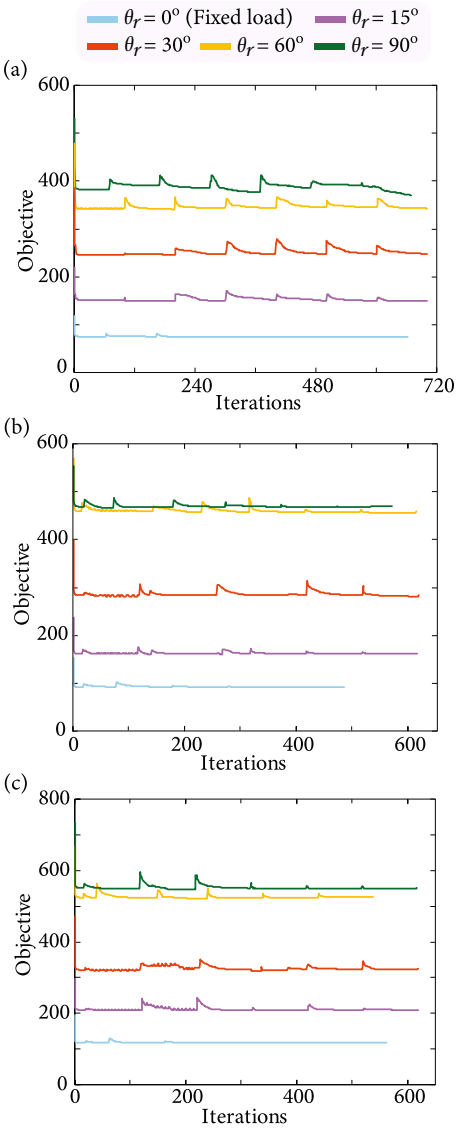

Fig. 24 Plot of the optimization convergence for the Hook domain example considering global and local volume constraints with one distributed load varying in direction, corresponding to Case #1 (Sect. 3.1, Fig. 11). **a** Global volume constraint. **b** Local volume constraint with 16 sub-regions. **c** Local volume constraint with 48 sub-regions

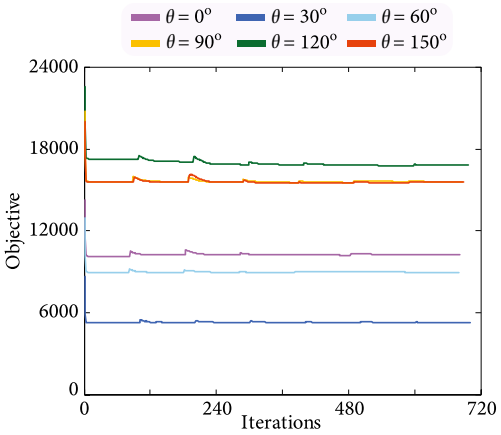

Fig. 25 Plot of the optimization convergence for the Pier cap beam domain example considering one distributed load with fixed directions (θ_1), and one distributed load varying in direction (θ_2), corresponding to Case #2 (Sect. 3.2, Fig. 15)

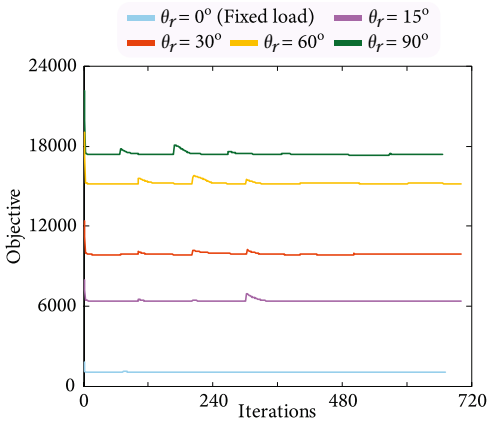

Fig. 26 Plot of the optimization convergence for the Pier cap beam domain example considering two distributed loads varying independently in direction (θ_1 and θ_2), corresponding to Case #3 (Sect. 3.3, Fig. 17)

Acknowledgements This work was partially funded by the National Science Foundation, United States (NSF) through Grant #2105811. The first author acknowledges support from the National Program of Scholarship and Educational Credit (PRONABEC) of the Ministry of Education of Peru.

Declarations

Conflict of interest The authors declare that they have no conflict of interest. The authors declare no competing interests.

Replication of results The numerical results presented in this document can be replicated using the methodology and formulations described here.

References

Allaire G, Michailidis G (2018) Modal basis approaches in shape and topology optimization of frequency response problems. Int J Numer Methods Eng 113:1258–1299. https://doi.org/10.1002/nme.5504

Asadpoure A, Tootkaboni M, Guest JK (2011) Robust topology optimization of structures with uncertainties in stiffness—application to truss structures. Comput Struct 89:1131–1141. https://doi.org/10.1016/j.compstruc.2010.11.004

Bendsøe MP, Kikuchi N (1988) Generating optimal topologies in structural design using a homogenization method. Comput Methods Appl Mech Eng 71:197–224. https://doi.org/10.1007/BF01650949

Bendsøe MP, Sigmund O (1999) Material interpolation schemes in topology optimization. Arch Appl Mech 69:635–654. https://doi.org/10.1007/s004190050248

Ben-Tal A, Nemirovski A (2002) Robust optimization-methodology and applications. Math Program 92:453–480. https://doi.org/10.1007/s101070100286

Csébfalvi A (2018) Structural optimization under uncertainty in loading directions: benchmark results. Adv Eng Softw 120:68–78. https://doi.org/10.1016/j.advengsoft.2016.02.006

da Silva Smith O (1997) Topology optimization of trusses with local stability constraints and multiple loading conditions-a heuristic approach. Struct Optim 13:155–166. https://doi.org/10.1007/BF01199235

Deng S, Suresh K (2017) Topology optimization under thermo-elastic buckling. Struct Multidisc Optim 55:1759–1772. https://doi.org/10.1007/s00158-016-1611-2

Diaz A, Bendsøe M (1992) Shape optimization of structures for multiple loading conditions using a homogenization method. Struct Optim 4:17–22. https://doi.org/10.1007/BF01894077

Dunning PD, Kim HA, Mullineux G (2011) Introducing loading uncertainty in topology optimization. AIAA J 49:760–768. https://doi.org/10.2514/1.J050670

Ferrari F, Sigmund O (2019) Revisiting topology optimization with buckling constraints. Struct Multidisc Optim 59:1401–1415. https://doi.org/10.1007/s00158-019-02253-3

Giraldo-Londoño O, Paulino GH (2020) A unified approach for topology optimization with local stress constraints considering various failure criteria: von Mises, Drucker–Prager, Tresca, Mohr–Coulomb, Bresler–Pister and William–Warnke. Proc R Soc A 476:20190861. https://doi.org/10.1098/rspa.2019.0861

Guest JK, Igusa T (2008) Structural optimization under uncertain loads and nodal locations. Comput Methods Appl Mech Eng 198:116–124. https://doi.org/10.1016/j.cma.2008.04.009

Guo X, Zhang W, Zhang L (2013) Robust structural topology optimization considering boundary uncertainties. Comput Methods Appl Mech Eng 253:356–368. https://doi.org/10.1016/j.cma.2012.09.005

Holmberg E, Torstenfelt B, Klarbring A (2014) Fatigue constrained topology optimization. Struct Multidisc Optim 50:207–219. https://doi.org/10.1007/s00158-014-1054-6

Holmberg E, Thore CJ, Klarbring A (2017) Game theory approach to robust topology optimization with uncertain loading. Struct Multidisc Optim 55:1383–1397. https://doi.org/10.1007/s00158-016-1548-5

Jalalpour M, Guest JK, Igusa T (2013) Reliability-based topology optimization of trusses with stochastic stiffness. Struct Saf 43:41–49. https://doi.org/10.1016/j.strusafe.2013.02.003

James KA, Hansen JS, Martins JR (2009) Structural topology optimization for multiple load cases using a dynamic aggregation technique. Eng Optim 41:1103–1118. https://doi.org/10.1080/03052150902926827

Jeong SH, Choi DH, Yoon GH (2015) Fatigue and static failure considerations using a topology optimization method. Appl Math Model 39:1137–1162. https://doi.org/10.1016/j.apm.2014.07.020

Jin M, Zhang X (2016) A new topology optimization method for planar compliant parallel mechanisms. Mech Mach Theory 95:42–58. https://doi.org/10.1016/j.mechmachtheory.2015.08.016

Lazarov BS, Schevenels M, Sigmund O (2012) Topology optimization with geometric uncertainties by perturbation techniques. Int J Numer Methods Eng 90:1321–1336. https://doi.org/10.1002/nme.3361

Lee E, James KA, Martins JR (2012) Stress-constrained topology optimization with design-dependent loading. Struct Multidisc Optim 46:647–661. https://doi.org/10.1007/s00158-012-0780-x

Li L, Khandelwal K (2017) Topology optimization of geometrically nonlinear trusses with spurious eigenmodes control. Eng Struct 131:324–344. https://doi.org/10.1016/j.engstruct.2016.11.001

Li H, Gao L, Li P (2014) Topology optimization of structures under multiple loading cases with a new compliance-volume product. Eng Optim 46:725–744. https://doi.org/10.1080/0305215X.2013.800054

Liu J, Wen G (2018) Continuum topology optimization considering uncertainties in load locations based on the cloud model. Eng Optim 50:1041–1060. https://doi.org/10.1080/0305215X.2017.1361417

Liu X, Li Z, Chen X (2011) A new solution for topology optimization problems with multiple loads: the guide-weight method. Sci China Technol Sci 54:1505–1514. https://doi.org/10.1007/s11431-011-4334-z

Lopes CG, Santos RBd, Novotny AA (2015) Topological derivative-based topology optimization of structures subject to multiple load-cases. Latin Am J Solids Struct 12:834–860. https://doi.org/10.1590/1679-78251252

Lu H, Tyas A, Gilbert M, Pichugin A (2021) On transmissible load formulations in topology optimization. Struct Multidisc Optim 64:23–37. https://doi.org/10.1007/s00158-021-02932-0

Picelli R, Townsend S, Brampton C, Norato J, Kim HA (2018) Stress-based shape and topology optimization with the level set method. Comput Methods Appl Mech Eng 329:1–23. https://doi.org/10.1016/j.cma.2017.09.001

Rong JH, Yu L, Rong XP, Zhao ZJ (2017) A novel displacement constrained optimization approach for black and white structural topology designs under multiple load cases. Struct Multidisc Optim 56:865–884. https://doi.org/10.1007/s00158-017-1692-6

Sá LF, Okubo CM Jr, Sá AN, Silva ECN (2022) Continuous boundary condition propagation model for topology optimization. Struct Multidisc Optim 65:15. https://doi.org/10.1007/s00158-021-03148-y

Sanders ED, Pereira A, Aguiló MA, Paulino GH (2018) PolyMat: an efficient MATLAB code for multi-material topology optimization. Struct Multidisc Optim 58:2727–2759. https://doi.org/10.1007/s00158-018-2094-0

Senhora FV, Giraldo-Londono O, Menezes IF, Paulino GH (2020) Topology optimization with local stress constraints: a stress aggregation-free approach. Struct Multidisc Optim 62:1639–1668. https://doi.org/10.1007/s00158-020-02573-9

Senhora FV, Sanders ED, Paulino GH (2022) Optimally-tailored spinodal architected materials for multiscale design and manufacturing. Adv Mater 34:2109304. https://doi.org/10.1002/adma.202109304

Senhora FV, Menezes IF, Paulino GH (2023) Topology optimization with local stress constraints and continuously varying load direction and magnitude: towards practical applications. Proc R Soc A 479:20220436. https://doi.org/10.1098/rspa.2022.0436

Spivak M (1965) Calculus on manifolds: a modern approach to classical theorems of advanced calculus. Benjamin, Inc., New York

Talischi C, Paulino GH, Pereira A, Menezes IF (2012) PolyTop: a MATLAB implementation of a general topology optimization framework using unstructured polygonal finite element meshes. Struct Multidisc Optim 45:329–357. https://doi.org/10.1007/s00158-011-0696-x

Thore CJ, Alm Grundström H, Klarbring A (2020) Game formulations for structural optimization under uncertainty. Int J Numer Methods Eng 121:165–185. https://doi.org/10.1002/nme.6204

Tootkaboni M, Asadpoure A, Guest JK (2012) Topology optimization of continuum structures under uncertainty—a polynomial chaos approach. Comput Methods Appl Mech Eng 201–204:263–275. https://doi.org/10.1016/j.cma.2011.09.009

Wang D, Gao W (2020) Robust topology optimization under multiple independent uncertainties of loading positions. Int J Numer Methods Eng 121:4944–4970. https://doi.org/10.1002/nme.6503

Wang F, Lazarov BS, Sigmund O (2011) On projection methods, convergence and robust formulations in topology optimization. Struct Multidisc Optim 43:767–784. https://doi.org/10.1007/s00158-010-0602-y

Xie Y, Steven GP (1994) Optimal design of multiple load case structures using an evolutionary procedure. Eng Comput 11:295–302. https://doi.org/10.1108/02644409410799290

Yi J, Rong J, Zeng T, Huang X (2013) A topology optimization method of multiple load cases and constraints based on element independent nodal density. Struct Eng Mech Int J 45:759–777. https://doi.org/10.12989/SEM.2013.45.6.759

Young V, Querin OM, Steven G, Xie YM (1999) 3D and multiple load case bi-directional evolutionary structural optimization (BESO). Struct Optim 18:183–192. https://doi.org/10.1007/BF01195993

Yun KS, Youn SK (2017) Multi-material topology optimization of viscoelastically damped structures under time-dependent loading. Finite Elem Anal Des 123:9–18. https://doi.org/10.1016/j.finel.2016.09.006

Zegard T, Paulino GH (2014) Grand-ground structure based topology optimization for arbitrary 2D domains using MATLAB. Struct Multidisc Optim 50:861–882. https://doi.org/10.1007/s00158-014-1085-z

Zhang W, Kang Z (2017) Robust shape and topology optimization considering geometric uncertainties with stochastic level set perturbation. Int J Numer Methods Eng 110:31–56. https://doi.org/10.1002/nme.5344

Zhang XS, Paulino GH, Ramos AS (2018) Multi-material topology optimization with multiple volume constraints: a general approach applied to ground structures with material nonlinearity. Struct Multidisc Optim 57:161–182. https://doi.org/10.1007/s00158-017-1768-3

Zhou K, Li X (2006) Topology optimization of structures under multiple load cases using a fiber-reinforced composite material model. Comput Mech 38:163–170. https://doi.org/10.1007/s00466-005-0735-9